Chemically induced fracturing in alkali feldspar

K. Scheidl[1], A.K. Schaeffer[1], E. Petrishcheva[1], G. Habler[1], F.D. Fischer[2], J. Schreuer[3], R. Abart[1]

July 9, 2013

[1] Department of Lithospheric Research, University of Vienna, A-1090 Vienna, Austria
[2] Institute of Mechanics, Montanuniversität Leoben, A-8700 Leoben, Austria
[3] Institute for Geology, Mineralogy and Geophysics, Ruhr-University Bochum, D-44801 Bochum, Germany

Abstract

Fracturing in alkali feldspar during Na^+-K^+ cation exchange with a NaCl-KCl salt melt was studied experimentally. Due to a marked composition dependence of the lattice parameters of alkali feldspar, any composition gradient arising from cation exchange causes coherency stress. If this stress exceeds a critical level fracturing occurs. Experiments were performed on potassium-rich gem quality alkali feldspars with polished (010) and (001) surfaces. When the feldspar was shifted towards more sodium-rich compositions over more than about 10 mole %, a system of parallel cracks with regular crack spacing formed. The cracks have a general (h0l) orientation and do not correspond to any of the feldspar cleavages. The cracks are rather oriented (sub)-perpendicular to the direction of maximum tensile stress. The critical stress needed to initiate fracturing is about 325 MPa. The critical stress intensity factor for the propagation of mode I cracks, K_{Ic}, is estimated at 2.30 to 2.72 MPa $m^{1/2}$ (73 to 86 MPa $mm^{1/2}$) from a systematic relation between characteristic crack spacing and coherency stress. An orientation mismatch of 18^o between the crack normal and the direction of maximum tensile stress is ascribed to the anisotropy of the longitudinal elastic stiffness which has pronounced maxima in the crack plane and a minimum in the direction of the crack normal.

Introduction

Feldspar is the most common mineral in the Earth's crust. It is an abundant rock forming mineral in igneous and metamorphic rocks and is also found as clastic and authigenic component in sediments. Fracturing in feldspar is a quite common phenomenon. Fracturing is important in a variety of geological processes. It determines the brittle strength, which is crucial in the context of jointing or cataclasis. During rock deformation at conditions of low and medium grade metamorphism feldspar usually yields by brittle failure (Paschier and Trouw 2005). Fracturing in feldspar is also common during fluid mediated mineral replacement (Jamtveit et al 2009). The resistance of a mineral against brittle failure is one of the most fundamental mechanical properties. There is a wealth of literature on fracturing of glass and ceramics. The data base for minerals is comparatively scarce. Broz et al (2006) and Whitney et al (2007) used an indentation technique for determining the so called fracture toughness of a number of rock-forming minerals. This method yields consistent data for the fracture toughness of the rock forming minerals, but the kinematics and mechanics of the fracturing process associated with indentation is rather complex, and quantifying fracture toughness from indentation tests may be ambiguous (Quinn and Bradt 2007). Furthermore, the indentation tests are usually done at ambient conditions and the mechanical data must be extrapolated over large ranges in temperature when applied to the analysis of the fracturing associated with deformation or fluid mediated alteration at high temperature. In this study we make use of the strongly anisotropic change in the lattice parameters that is associated with composition change in alkali feldspar to estimate the critical stress that is necessary for creating mode I cracks. To this end we analyze the crack patterns forming during Na^+-K^+ exchange between alkali feldspar and a salt melt without application of externally imposed stress. Our approach entirely relies on the elastic stress associated with the eigenstrain due change during cation exchange, and in this respect it is complementary to mechanical testing by indentation.

Most feldspars pertain to the ternary solid-solution series among the end-member components $NaAlSi_3O_8$ (albite), $KAlSi_3O_8$ (orthoclase), and $CaAl_2Si_2O_8$ (anorthite). The feldspars belong to the group of framework silicates where an $(AlSi_3O_8)$-network is formed by corner-shared TO_4 tetrahedra with T = Al, Si. The Na^+, K^+, and Ca^{2+} cations, which ensure charge balance, are located in large, irregular cavities of the tetrahedral framework (Ribbe, 1986).

The two end-member components of the alkali feldspar solid-solution series, albite and orthoclase, are related through Na^+-K^+ cation exchange. Misci-

bility in the alkali feldspars is complete at temperatures exceeding 550^{o}C to 800^{o}C, depending on pressure (Brown and Parsons, 1988). At lower temperatures a miscibility gap opens leading to separation of alkali feldspar with intermediate composition into a sodium- and a potassium-rich phase (perthite formation). During cooling, heating or composition change the alkali feldspars undergo a variety of phase transformations and structural changes including a ferroelastic monoclinic - triclinic transformation, Al-Si ordering on the tetrahedral sites, and exsolution. Due to the complex sub-solidus phase relations the alkali feldspars show a wide variety of intracrystalline microstructures and textures, which potentially bear petrogenetic information (Smith and Brown 1986). Experimental calibrations of the equilibrium phase relations in binary alkali feldspars (Thompson and Waldbaum 1968; Hovis et al. 1991) and in the ternary feldspar system (Fuhrman and Lindsley 1988; Benisek et al. 2010) have provided the basis for two-feldspar-thermometry. The thermodynamics of alkali feldspar solid solutions was coupled with diffusion kinetics to derive quantitative models for the dynamics of phase separation during perthite formation (Yund 1984, Petrishcheva and Abart 2009, 2012; Abart et al. 2009 a,b).

The lattice dimensions of the alkali feldspars are composition dependent (Kroll et al. 1986; Angel et al. 2012). As a consequence, any chemical heterogeneity in a feldspar single crystal leads to coherency stress. The associated strain energy contributes positively to the free energy and thus counteracts exsolution (Robin 1974). As a consequence, a coherent solvus and the corresponding strain free solvus are discerned; where the miscibility gap extends to higher temperature in the strain free case than in the coherent case (Brown and Parsons 1988). Coherency strain does not only affect the equilibrium phase relations, but it can also influence microstructure evolution. For instance, the exsolution lamellae in a perthite are oriented such that the interface energy between host and precipitate is minimized (Bollmann and Nissen 1968; Robin 1974).

Petrovic (1973) and Neusser et al. (2012) observed fracturing in alkali feldspar during Na^+-K^+ cation exchange with NaCl-KCl salt melt, which they interpreted as coherency stress effects. Neusser et al. (2012) presented a mechanical analysis of the stress state in a thin misfitting layer on a (010) surface of an alkali feldspar and concluded that cracks formed sub-perpendicular to the direction of maximum tensile stress.

In this communication we address chemically induced fracturing in alkali feldspar. We focus on crack patterns that form during Na^+-K^+ cation exchange in samples with well-defined starting geometry. The treatment of Neusser et al. (2012) is extended to the stress analysis on a (001) surface and use is made of the regularity of the system of parallel cracks emanating from

polished (010) and (001) surfaces to attain insight into the fracture mechanics. We fully confirm the observations made earlier by Neusser et al. (2012) and provide more quantitative relations between coherency stress induced by cation exchange and fracturing.

Experimental

Starting material

Gem-quality sanidines from two different localities in the Eifel, Volkesfeld and Rockeskyller Kopf, were used as starting materials. The composition of sanidine from Volkesfeld can be described as $Or_{84}Ab_{15}Cs_{01}$ whereas the sanidine from the Rockeskyller Kopf is more sodium-rich with a composition of $Or_{72}Ab_{26}Cs_{02}$ (see Table 1). Both sanidines are characterized as monoclinic with space group C2/m, disordered (Al, Si) distribution ($\Sigma t1 =$ 61: Volkesfeld, $\Sigma t1 = 0.58$ - 0.62: Rockeskyll) and are homogenous on the nanometer scale (Neusser et al. 2012; Demtroeder 2011). The crystals are optically clear and, apart from the (010) and (001) cleavages, devoid of cracks or any other flaws.
Two different sets of experiments were performed. On the one hand, crystal fragments obtained from crushing and sieving to a size of 100 - 200 μm were used to determine the critical composition shift needed to initiate fracturing on the (010) and (001) cleavage planes. On the other hand, crystals were machined to plates of 3 mm by 3 mm by 1 mm with polished (001) or (010) faces for later use in experiments, where well-defined starting geometry is important.

Cation exchange experiments

The Na^+-K^+ exchange experiments were done between alkali felspar and an NaCl-KCl salt melt at close to ambient pressure and without adding a fluid. About 0.1 g of crushed feldspar or one feldspar plate together with a NaCl-KCl salt mixture was sealed into quartz glass tubes with an outer diameter of 9 mm and an inner diameter of 7 mm under vacuum. The NaCl/KCl ratio of the salt mixture was chosen to produce the desired chemical shift of the alkali feldspar based on the Na/K fractionation data for feldspar - salt-melt equilibria at 850^{o}C (Neusser et al. 2012). To ensure a constant composition of the salt melt during the exchange experiments a 40-fold molar excess of Na^+ and K^+ cations in the salt relative to the feldspar was applied. The samples were then annealed under ambient pressure at 850^{o}C in a muffle furnace for

7 to 8 days (see Tables 2 and 3). After annealing the samples were quenched in cold water within seconds. Then the tubes were opened, the salt was dissolved with deionized water and the feldspar was quantitatively retrieved. Grain mounts were prepared from the crystal fragments and the feldspar plates were cut perpendicular to the polished surfaces and embedded in resin for preparation of polished sections.

Analytical Techniques

Scanning electron microscopy

For BSE imaging an FEI Inspect S scanning electron microscope with a tungsten filament was used. The images were taken at 10 kV and 15 kV beam acceleration voltage and 8 nA beam current.
Electron back scatter diffraction (EBSD) analyses were performed using a FEI Quanta 3D FEG instrument at the Department of Lithospheric Research (University of Vienna, Austria). The system is equipped with a field-emission electron source and an EDAX Digiview IV EBSD camera. The software packages OIM Data Collection and Analysis have been applied for EBSD data acquisition and processing. Prior to analysis single crystals were embedded in epoxy resin, then first polished mechanically and subsequently chemo-mechanically using a colloidal silica suspension with pH 9.2-10 as polishing agent on a rotary polisher. Conductivity of the sample surface was established by thin carbon coating using a single carbon thread at a distance of about 8 cm between thread and sample at vacuum conditions of $< 10^{-5}$ mbar during evaporation. For EBSD-analyses a working distance of 12 mm or 14 mm and a sample tilt of 70^o were applied. The edges of the crystals were aligned parallel to the x- and y-directions of the scan reference system by stage rotation. The electron-beam settings were 15 kV accelerating voltage and 4 nA beam current in analytical mode (SEM aperture 1 mm). A 2 by 2 or 4 by 4 binning of the EBSD camera-resolution was applied, and the camera exposure time and pattern contrast enhancement settings were adjusted for each grain according to the pattern quality. Hough settings of 1^o 2θ step size, a binned pattern size of 160 pixels and a minimum peak distance of 10 degrees were applied for indexing 6 - 14 Hough peaks. A medium (9 by 9) or large (13 by 13) convolution mask was applied to the Hough space in order to eliminate artifacts and enhance weak bands. Only the interior portion of the EBSD pattern (ρ-fraction = 70% to 85% of the Hough space) was used for indexing. EBSD mapping was performed by beam scanning across a 100 μm by 100 μm or 150 μm by 150 μm sized sample area of each crystal using a

step size of 15 μm. Thus 45 - 100 data points were collected for each crystal. In case of inconsistent indexing results for single maps the data statistics as well as the different solutions for single point analyses were checked in order to detect the misindexed data points. All pole figures displayed in this work refer to the upper hemisphere.

Mineral chemical analysis and element mapping

Mineral chemical analyses and element mapping were done on a Cameca SX 100 electron microprobe at the Department of Lithospheric Research (University of Vienna, Austria). The elements Na, K, Fe, Ba, Mg, Al, Si were considered in mineral chemical analysis. The standards and spectrometer settings are listed in Table 4. An acceleration voltage of 15 kV and a beam current of 20 nA were applied. A 6 μm defocussed beam was used to minimize loss of Na by evaporation. For element mapping of Na, K, Al, Ba and Si an accelerating voltage of 10 kV, a beam current of 50 nA, a dwell time of 60 ms per pixel, and stage scanning mode with 0.6 μm step size were used.

Results

Characteristics of the cracks

When a grain of alkali feldspar is exposed to a NaCl-KCl salt-melt Na^+-K^+ cation exchange produces a chemically altered zone on the surface of the grain, and the alteration front progresses into the grain interior with time. Associated with the chemical change is the formation of cracks. As already described by Neusser et al. (2012) two fundamentally different crack patterns form depending on the direction of composition shift (see Figure 1).
When the feldspar is shifted towards more sodium-rich compositions a regular hierarchical pattern of cracks forms (Figure 1a). The first hierarchical level is represented by a system of sub-parallel cracks, which extend approximately parallel to a (h0l) plane. These cracks are not perfectly planar but are somewhat uneven. They enclose an angle of 8^o - 18^o with the positive *c*-axis, measured towards the positive *a*-axis. This corresponds to an angle of 73^o - 83^o with the negative *a*-axis measured towards the positive *c*-axis, given that $\beta = 116^o$ (see Figures 2 and 3). It is important to note that the cracks follow a general plane in the feldspar lattice, which is not related to any of the cleavages. Chemical alteration extends into the grain interior along the cracks (see Figure 4) indicating that the cracks formed during cation exchange and cannot be interpreted as quench phenomena. The

observed chemical patterns suggest that the salt melt penetrated into the grain interior along the cracks and chemical alteration further spread into the crystal from the crack surfaces. The cracks of the second hierarchical level are perfectly straight and run parallel to the (010) and (001) cleavages (see Figure 1a). These cracks are devoid of any alteration haloes indicating that they formed very late during the experiment and may be interpreted as quenching-effects. The orientation of the cracks slightly differs between the Volkesfeld sanidine and the sanidine from the Rockeskyller Kopf. For the sanidine from Volkesfeld with its original $X_{Or} = 0.84$ the angle between the cracks and the negative a-axis is measured as 83^o (σ= 2.0^o; 48 measurements in 3 samples), and for the sanidine from the Rockeskyller Kopf with its original $X_{Or} = 0.72$ the angle is 73^o ($\sigma = 2.8^o$; 33 measurements in 2 samples). During the incipient stages of cation exchange a few short cracks emanate perpendicular to the surface of the grains. With increasing run duration the number of cracks increases, the cracks become longer and they are deflected into the common (h0l) plane. Eventually no more cracks develop; at this stage a characteristic crack spacing between 10-50 μm has been established, depending on the extent of composition shift (see below).
In contrast, when the sanidine is shifted towards more potassium-rich compositions a potassium-enriched rim develops, which is separated from the unaltered grain interior by a more or less diffuse transition zone. The lattice parameters in the potassium-enriched rim are larger than in the unaltered substratum. The lattice mismatch leads to coherency stress and eventually cracks form along the transition zone between core and rim, a phenomenon that is particularly pronounced at the grain edges (Figure 1b).

Critical shift for fracturing

To identify the critical composition shift needed to initiate fracturing fragments of crushed sanidine with initial $X_{Or} = 0.84$ were exchanged with NaCl-KCl salt-melt at 850^oC for 7 days. The X_{KCl} of the salt-mixture was varied from 0.35 to 0.31 in 1 mole % steps to achieve successively increasing composition shifts towards more sodium-rich compositions in the feldspar (see Table 2). The first cracks formed on the (010) and (001) (cleavage) surfaces, when X_{KCl} was 0.34 corresponding to an exchanged feldspar with $X_{Or} = 0.71$. The first cracks were thus observed when the original feldspar was shifted over 13 mole % from its original composition.

Dependence of the crack spacing on the chemical shift

It was already noted qualitatively by Neusser et al. (2012) that the characteristic crack spacing decreases with increasing extent of chemical shift, i.e. with increasing coherency stress between the unaltered and the exchanged portions of the crystal. This relation could, however, not be verified quantitatively by the latter authors, because only crystal fragments were investigated where the fracture patterns were substantially influenced by irregularities on the grain surface. In our investigation crystal plates with polished (001) or (010) faces were used to avoid the influence of surface topography on the nucleation of cracks. The initial compositions of the crystals were $X_{Or} = 0.84$ and $X_{Or} = 0.72$, and the NaCl/KCl ratio of the salt-melt was varied systematically to attain composition shifts between 20 mole % and 55 mole %. The run durations were varied between 8 days and 32 days. The long time runs produced rather complex crack patterns and only the results from 8 day experiments were used for establishing the relation between crack spacing and chemical shift (see Table 3).

Figures 6 and 7 show the system of parallel cracks emanating from the polished (010) and (001) surfaces of sanidine from Volkesfeld and from the Rockeskyller Kopf, respectively. The crystals were mounted in resin in such a way that the polished surfaces of the crystals, either (010) or (001), were oriented perpendicular to the surface of the mount. The crystal orientations were determined using EBSD and the corresponding pole figures are shown as inserts. As the cracks run parallel to a (h0l) plane they are always perpendicular to the polished (010) surfaces of the crystals, and the traces of the cracks that are visible on the surface of a particular sample are perpendicular to the trace of the polished (010) surface of the crystal. In general, the cracks are, however, not perpendicular to the surface of the polished mount, and the spacing between the traces of the cracks does not correspond to the actual spacing between the cracks. We denote the observed spacing between the crack traces as h'. Given that the crystal orientation has been determined from EBSD analyses and the true angle φ of intersection between the cracks and the (001) surface is known ($\varphi = 83^o$ for the sanidine from Volkesfeld, and $\varphi = 73^o$ for the sanidine from the Rockeskyller Kopf) the true angle ϵ between the sample surface and the cracks can be determined. The crack spacing h is then obtained from ϵ and h' according to

$$h = \sin\epsilon \cdot h'.$$

In samples where crystals with polished (001) faces have been mounted the traces of the cracks are generally not perpendicular to the traces of the polished (001) planes, and the observed spacing between the traces of the cracks

differs from the actual crack spacing. Again, we denote the spacing between the crack traces as h', and we denote the angle between the crack traces and the trace of the (001) surface as φ'. Given that φ the true angle of intersection between the cracks and the (001) surface is known, the actual crack spacing h is determined from the observed h' and φ' according to

$$h = \frac{\cos\varphi}{\cos\varphi'} \cdot h'.$$

The cracks emanating from the polished surfaces show a very regular spacing. In Figure 5 the crack spacing is plotted as a function of composition shift. The crack spacing systematically decreases with increasing composition shift for both sanidines and for cracks emanating from both the (010) and (001) faces.

Discussion

Stress in a thin misfitting layer on a planar surface

It is inferred from the experimental evidence that formation of the cracks is related to the shift in composition caused by Na^+-K^+ exchange. Although chemically induced fracturing is observed with both directions of chemical shift, we restrict our analysis to the case with the chemical shift towards more sodium-rich compositions. This is due to the fact that regular crack patterns with simple geometry only occur in this case and based on a straightforward mechanical analysis material properties can be extracted from the observed crack patterns. The cracks produced by shifts towards more potassium-rich compositions have irregular shape and extracting material parameters from an inverse approach does not appear to be feasible. Numerical forward modeling could potentially reproduce the observed crack patterns, for such modeling the material properties would have to be known as input parameters though.

The lattice parameters of alkali feldspar depend on composition. A shift of a potassium-rich alkali feldspar towards more sodium-rich compositions leads to an anisotropic contraction of the lattice and a change in the angle β. We only consider composition shifts small enough to ensure that the monoclinic symmetry is preserved. The lattice contraction is most pronounced in the a-direction and by a factor of about five smaller along the b- and c- directions (Kroll and Ribbe 1983; Kroll et al. 1986). During Na^+-K^+ exchange a zone in equilibrium with the salt melt develops at the grain surface and successively spreads into the grain interior by the interdiffusion of Na^+ and K^+ on the

alkali sublattice. Along the transition zone between the exchanged rim and the grain's interior the concentration of the cations varies while the tetrahedral framework remains coherent. This produces elastic strain and therefore coherency stress that compensates for the lattice misfit. If this coherency stress exceeds a critical value, fracturing is initiated. Cracks start to form at an early stage of cation exchange when only a thin layer of chemically altered feldspar has been produced at the grain surface. At this stage the unaltered domain in the grain interior is volumetrically by far dominant and, as a consequence, mechanically much stiffer than the thin misfitting surface layer. In this situation, the elastic strain and the associated coherency stress are localized in the thin misfitting surface layer. The unaltered substrate may be approximated as rigid.
The mechanical analysis of the stress state associated with the development of a thin misfitting layer due to composition change at the surface of a rigid substrate involves two basic tasks: Firstly, the eigenstrain due to composition change is calculated from the composition dependent change in lattice parameters. Secondly, the elastic stress induced by the eigenstrain due to composition change is calculated for specific boundary conditions that reflect the orientation of the surface. We will restrict our analysis to planar surfaces of a monoclinic crystal.

Eigenstrain by composition change

As usual, we describe the crystal lattice with three vectors **a**, **b**, and **c**, where for the monoclinic system under consideration **b** is the diad axis and $\alpha = \gamma = 90^o$ and $\beta > 90^o$. We employ the orthogonal coordinate system $Oxyz$ generated by **a**, **b**, and $\mathbf{c}^\star$, where $\mathbf{c}^\star \parallel \mathbf{a} \times \mathbf{b}$. Let the composition induced change in lattice parameters in a monoclinic alkali feldspar be (see Figure 8)

$$a_0,\ b_0,\ c_0,\ \beta_0 \quad \rightarrow \quad a_1,\ b_1,\ c_1,\ \beta_1.$$

According to the monoclinic symmetry we have for the corresponding eigenstrain tensor, ε_{ij}

$$\varepsilon_{ij} = \begin{pmatrix} \varepsilon_{11} & 0 & \varepsilon_{13} \\ 0 & \varepsilon_{22} & 0 \\ \varepsilon_{13} & 0 & \varepsilon_{33} \end{pmatrix},$$

with (for a detailed derivation see the appendix)

$$\varepsilon_{11} = \frac{a_1}{a_0} - 1,$$
$$\varepsilon_{22} = \frac{b_1}{b_0} - 1,$$
$$\varepsilon_{33} = \frac{c_1 \sin\beta_1}{c_0 \sin\beta_0} - 1,$$
$$\varepsilon_{13} = \frac{c_1 \cos\beta_1}{2c_0 \sin\beta_0} - \frac{a_1 \cos\beta_0}{2a_0 \sin\beta_0}.$$

The composition dependence of the lattice parameters for disordered alkali feldspar was documented by Kroll et al. (1986). We use the lattice parameters that are given by the latter authors for the compositions $X_{Or} = 0.84$ and $X_{Or} = 0.69$ (see Table 5), because they most closely represent the composition range of interest in the context of our experiments. Based on these data, we obtain $\varepsilon_{11} = -7.6 \times 10^{-3}$, $\varepsilon_{22} = -5.1 \times 10^{-4}$, $\varepsilon_{33} = -5.9 \times 10^{-4}$, $\varepsilon_{13} = -1.9 \times 10^{-3}$ for a composition shift of $X_{Or} = 0.84 \rightarrow 0.69$.

Stress and strain in a thin misfitting layer on a (010) surface

We now consider formation of a thin misfitting layer on a (010) surface of monoclinic alkali feldspar. The geometry of the system to be analyzed is shown schematically in figure 9. We follow the analysis of Neusser et al. (2012) and only a brief summary of the approach is given here. The total strain ε_{ij}^{tot} results from a combination of the eigenstrain due to composition change ε_{ij} and elastic strain ε_{ij}^{el}

$$\varepsilon_{ij}^{tot} = \varepsilon_{ij} + \varepsilon_{ij}^{el}. \quad (1)$$

When a thin misfitting layer forms on a (010) surface of a stiff, i.e. formally rigid alkali feldspar substratum, coherency of the tetrahedral framework across the transition zone requires that the in-plane components of the total strain vanish, i.e. $\varepsilon_{11}^{tot} = \varepsilon_{33}^{tot} = \varepsilon_{13}^{tot} = 0$ (see Figure 9). The components ε_{12}^{tot} and ε_{23}^{tot} vanish because of the monoclinic symmetry. Applying equation (1) we obtain for the elastic strain tensor $\varepsilon_{ij}^{el} = \varepsilon_{ij}^{tot} - \varepsilon_{ij}$

$$\varepsilon_{ij}^{el} = \begin{pmatrix} -\varepsilon_{11} & 0 & -\varepsilon_{13} \\ 0 & \varepsilon_{22}^{el} & 0 \\ -\varepsilon_{13} & 0 & -\varepsilon_{33} \end{pmatrix}.$$

The strain component ε_{22}^{el} remains unspecified and must be calculated from additional constraints. We introduce Voigt notation

$$\varepsilon_{ij}^{el} \rightarrow \varepsilon_{i}^{el},$$

where the indices transform as: 11 → 1, 22 → 2, 33 → 3, 23, 32 → 4, 13, 31 → 5, 12, 21 → 6 (see Figure 9). According to Hooke's law we have

$$\sigma_i = c_{ij}\varepsilon_j^{\mathrm{el}}, \tag{2}$$

where

$$\sigma_i = \begin{pmatrix} \sigma_1 \\ \sigma_2 \\ \sigma_3 \\ \sigma_4 \\ \sigma_5 \\ \sigma_6 \end{pmatrix} \quad \text{and} \quad \varepsilon_j^{\mathrm{el}} = \begin{pmatrix} \varepsilon_1^{\mathrm{el}} \\ \varepsilon_2^{\mathrm{el}} \\ \varepsilon_3^{\mathrm{el}} \\ \frac{1}{2}\varepsilon_4^{\mathrm{el}} \\ \frac{1}{2}\varepsilon_5^{\mathrm{el}} \\ \frac{1}{2}\varepsilon_6^{\mathrm{el}} \end{pmatrix}$$

are the components of stress and elastic strain, and c_{ij} is the matrix of elastic constants, respectively, in Voigt notation, and Einstein summation is implied. As cation exchange took place in a liquid environment, i.e. no shear stresses are transferred, and at close to ambient pressure, the out of plane stress components on the crystal surface vanish, and we have $\sigma_2 = \sigma_4 = \sigma_6 = 0$. Applying equations (1) and (2) we obtain a system of linear equations

$$\begin{pmatrix} \sigma_1 \\ 0 \\ \sigma_3 \\ 0 \\ \sigma_5 \\ 0 \end{pmatrix} = \begin{pmatrix} c_{11} & c_{12} & c_{13} & 0 & c_{15} & 0 \\ c_{21} & c_{22} & c_{23} & 0 & c_{25} & 0 \\ c_{31} & c_{32} & c_{33} & 0 & c_{35} & 0 \\ 0 & 0 & 0 & c_{44} & 0 & c_{46} \\ c_{51} & c_{52} & c_{53} & 0 & c_{55} & 0 \\ 0 & 0 & 0 & c_{64} & 0 & c_{66} \end{pmatrix} \begin{pmatrix} -\varepsilon_1 \\ \varepsilon_2^{\mathrm{el}} \\ -\varepsilon_3 \\ 0 \\ -\frac{1}{2}\varepsilon_5 \\ 0 \end{pmatrix}.$$

Four of the six equations are independent, they can be solved to provide the unknown stresses σ_1, σ_3, σ_5, and the unknown elastic strain $\varepsilon_2^{\mathrm{el}}$. We interpolate the elastic constants for monoclinic alkali feldspar given by Schreuer et al. (in prep.) for $T = 850^\circ$ C (see Table 6). For the composition change of $X_{\mathrm{Or}} = 0.84 \rightarrow 0.69$ we obtain the stress

$$\sigma_{ij}/\mathrm{GPa} = \begin{pmatrix} 0.39 & 0 & -0.025 \\ 0 & 0 & 0 \\ -0.025 & 0 & 0.27 \end{pmatrix}$$

and the elastic strain

$$\varepsilon_{ij}^{\mathrm{el}} = \begin{pmatrix} 0.076 & 0 & 9.6 \times 10^{-4} \\ 0 & -0.0021 & 0 \\ 9.6 \times 10^{-4} & 0 & 5.9 \times 10^{-4} \end{pmatrix},$$

again adopting tensor notation. According to the monoclinic symmetry of the feldspar only the σ_2 principle axis of the stress tensor is parallel to the $\varepsilon_2^{\mathrm{el}}$

principle axis of the elastic strain tensor, and they are both parallel to the crystallographic b axis (diad axis). The σ_1 and σ_3 principle axes of the stress tensor and the $\varepsilon_1^{\rm el}$ and $\varepsilon_3^{\rm el}$ principle axes of the strain tensor lie in the $a-c$ plane. They are, however, in general not parallel to the crystallographic a or c axes, neither are the principle axes of the stress and the strain tensors parallel to each other. The principle components of the stress tensor and the direction of principle axes are given by the well-known relations (Nye 1995)

$$\sigma_1 = \frac{\sigma_{11}+\sigma_{33}}{2} + \sqrt{\left(\frac{\sigma_{11}+\sigma_{33}}{2}\right)^2 + \sigma_{13}^2} = 0.40\,\text{GPa},$$

$$\sigma_3 = \frac{\sigma_{11}+\sigma_{33}}{2} - \sqrt{\left(\frac{\sigma_{11}+\sigma_{33}}{2}\right)^2 + \sigma_{13}^2} = 0.27\,\text{GPa},$$

$$\phi = \frac{1}{2}\arctan\frac{2\sigma_{13}}{\sigma_{11}-\sigma_{33}} = 11.72^\circ.$$

The representation quadric of the derived stress tensor is shown in Figure 10. The crack direction is roughly perpendicular to the σ_1 principle axis of the stress. The latter corresponds to the largest principle component σ_1, i.e. to the maximum tensile stress. Noting that fracturing is first initiated after a composition shift of 0.13 X_{Or}, the critical tensile stress that is needed to initiate fracturing on a (010) surface of alkali feldspar is derived from the above example, which was calculated for a composition shift of 0.16 X_{Or}, as $\sigma_{1c} = 0.13/0.16\ \sigma_1 = 0.325$ GPa.

Stress and strain in a thin misfitting layer on a (001) surface

We now investigate the strain and associated stress induced by chemical change in a thin layer on a (001) surface of monoclinic alkali feldspar. The conditions for the total stress imposed on a thin misfitting layer on a (001) surface through a coherent contact with a mechanically stiff, i.e. formally rigid substratum are $\varepsilon_{11}^{\rm tot} = \varepsilon_{22}^{\rm tot} = \varepsilon_{12}^{\rm tot} = 0$ (see Figure 9). Applying again equation (1) and noting that $\varepsilon_{12}^{\rm tot} = \varepsilon_{23}^{\rm tot} = 0$ because of the monoclinic symmetry we have for the elastic strain tensor

$$\varepsilon_{ij}^{\rm el} = \begin{pmatrix} -\varepsilon_{11} & 0 & \varepsilon_{13}^{\rm el} \\ 0 & -\varepsilon_{22} & 0 \\ \varepsilon_{13}^{\rm el} & 0 & \varepsilon_{33}^{\rm el} \end{pmatrix}.$$

In this case, two strain components $\varepsilon_{13}^{\rm el}$ and $\varepsilon_{33}^{\rm el}$ must be calculated from additional constraints. Again, due to the fact that the chemical alteration took place in a liquid under a pressure of less than one atmosphere the out of

plane stress components vanish and $\sigma_{13} = \sigma_{23} = \sigma_{33} = 0$. Applying Hooke's law (in Voigt notation) we obtain a system of linear equations

$$\begin{pmatrix} \sigma_1 \\ \sigma_2 \\ 0 \\ 0 \\ 0 \\ \sigma_6 \end{pmatrix} = \begin{pmatrix} c_{11} & c_{12} & c_{13} & 0 & c_{15} & 0 \\ c_{21} & c_{22} & c_{23} & 0 & c_{25} & 0 \\ c_{31} & c_{32} & c_{33} & 0 & c_{35} & 0 \\ 0 & 0 & 0 & c_{44} & 0 & c_{46} \\ c_{51} & c_{52} & c_{53} & 0 & c_{55} & 0 \\ 0 & 0 & 0 & c_{64} & 0 & c_{66} \end{pmatrix} \begin{pmatrix} -\varepsilon_1 \\ -\varepsilon_2 \\ \varepsilon_3^{\mathrm{el}} \\ 0 \\ \frac{1}{2}\varepsilon_5^{\mathrm{el}} \\ 0 \end{pmatrix},$$

which can be solved for the unknowns σ_1, σ_2, σ_6, $\varepsilon_3^{\mathrm{el}}$ and $\varepsilon_5^{\mathrm{el}}$. For the composition change of $X_{\mathrm{Or}} = 0.84 \rightarrow 0.69$ we obtain again adopting tensor notation

$$\sigma_{ij}/\mathrm{GPa} = \begin{pmatrix} 0.42 & 0 & 0 \\ 0 & 0.38 & 0 \\ 0 & 0 & 0 \end{pmatrix},$$

and

$$\varepsilon_{ij}^{\mathrm{el}} = \begin{pmatrix} 7.58 \times 10^{-3} & 0 & -2.34 \times 10^{-3} \\ 0 & 5.07 \times 10^{-4} & 0 \\ -2.34 \times 10^{-3} & 0 & -2.31 \times 10^{-3} \end{pmatrix}.$$

The diagonal form of σ implies that the principal axes of the stress tensor coincide with the axes of the orthogonal coordinate system. The maximum tension stress is represented by σ_{11}, i.e. it is parallel to the x-direction.. The cracks in the (001) surface are indeed perpendicular to the x-direction.

Fracture mechanics

One can assume that several crack nuclei (e.g. defects) are distributed on the surfaces of the specimen, especially along the edges, providing sites from where cracks can propagate through the chemically altered surface layer. Cracks form only when the chemical shift towards more sodium-rich compositions is 13 mole % or more. Referring to our stress analysis, this corresponds to a critical tensile stress of about 325 MPa that is necessary to induce fracturing. Cracks emanating from the (001) surface are exactly perpendicular to the direction of the maximum tensile stress on this surface, and they may thus be regarded as pure mode I cracks. With cracks emanating from the (010) surface the crack normal and the direction of maximum tensile stress enclose an angle of about 18^o. If the stress is resolved on the crack plane, a shear stress component parallel to the line of the crack tip results, and the cracks only approximately correspond to mode I with a minor component of mode III (out of plane shear component). The experimental observation

shows a system of parallel cracks that emanate from the surfaces and propagate through the entire specimen with time. It is intuitive to assume that fracturing is due to the tensile stress that is localized in the misfitting surface layer and the following analysis builds on the simplifying assumption that a homogeneous tensile stress in the surface layer provides the only driving force for fracturing. The analysis does, however, not account for the fact that chemical exchange also takes place at the crack surfaces (see Figure 4). The envelopes of altered feldspar accompanying the cracks have an influence on the stress field at the crack tip and provide additional driving force for crack propagation. Considering this effect is beyond the scope of this communication. Our analysis thus can only deliver A rough estimate for the parameter characterizing the fracture mechanics.

A number of fracturing criteria have been considered for brittle solids including concepts based on crystal structure, bond density and bond strength, elastic moduli and surface energy (Schultz et al. 1994). Each of these concepts provides reasonable fracture criteria for specific materials, but none is universally applicable. The latter authors suggested the stress intensity factor, which is a measure for the stress field around a crack tip, as the most suitable parameter for describing fracturing. With regard to our samples, it is important to note that the spacing of the cracks emanating from the polished surfaces is quite constant for a given composition shift and that the characteristic spacing varies systematically with the extent of composition shift. We also note that the stress induced in the thin, misfitting layer is directly proportional to the eigenstrain due to composition shift. Our observation thus documents a relation between the crack spacing and the induced stress. From this line of evidence we infer that the crack spacing is primarily controlled by the induced stress rather than by the occurrence of pre-existing randomly distributed defects, which would produce a more irregular crack pattern. We make use of the observed relation between the extent of composition shift and characteristic crack spacing to estimate the critical value of the stress intensity factor K_{Ic}, which may also be referred to as the "fracture toughness", for mode I cracks. In all crack patterns that we produced the relation between crack length a and crack spacing $2h$ is so that the crack spacing factor $s = a/(a+h) > 0.25$. According to Tada et al. (2000) (p. 264, Part III) the corresponding stress intensity factor for mode I cracks in this regime is

$$K_I \approx \sigma\sqrt{h}, \tag{3}$$

with the stress σ acting along the edge, i.e. orthogonal to the cracks. The observed relation between crack spacing and chemical shift, i.e. between crack spacing and coherency stress nicely reflects this proportionality (see Fig-

ure 5). For the cracks emanating from the (001) surface of sanidine from Volkesfeld, a fit of equation (3) to the data given in table 3 yields an estimate of $K_{Ic} = 2.72$ MPa m$^{1/2}$/86 MPa mm$^{1/2}$. The corresponding estimate for cracks emanating from the (010) surface is $K_{Ic} = 2.30$ MPa m$^{1/2}$/73 MPa mm$^{1/2}$. These estimates are different from what was found by Broz et al (2006) and by Whitney et al (2007) using an indentation technique for measuring the fracture toughness of rock forming minerals. Thereby the fracture toughness is determined from the length of radial cracks emanating from the corners of a load mark produced with a Vickers indenter. For orthoclase single crystals an indentation fracture toughness of 0.88 $\pm$ 0.13 MPa m$^{1/2}$ (Broze et al. 2006) and of of 1.1 $\pm$ 0.4 MPa m$^{1/2}$ (Whitney et al. 2007) was found, which is considerably lower than the values obtained in our study. Bernardo et al (2007) give an indentation fracture toughness of 1.5 to 2.0 for sintered $KAlSi_3O_8$ glass ceramics, the indentation fracture toughness for aluminium-oxide ceramics is 3 to 5 MPa m$^{1/2}$. There are several possible reasons for the discrepancy between the toughness estimates from this study and those from Broz et al (2006) and Whitney et al (2007). The cracks associated with the load mark of a Vickers indenter have a complex 3D geometry. No analytical solution exists for the associated stress field, and the "fracture toughness" obtained from indentation experiments merely rests on an empirical relation among the length of radial cracks from indentation, the applied load, the indentation hardness, and the elastic modulus, but it does not directly confer to the continuum mechanical definition of the stress intensity factor (Quinn and Bradt 2007). The nature (mode I, II, or III) of the cracks produced from indentation is not well defined, but the continuum mechanical definition of the stress intensity factor clearly discerns a K_I, K_{II}, and K_{III} for mode I, mode II, and mode III cracks, respectively (Quinn and Bradt 2007). The "indentation fracture toughness" is thus not directly comparable to the critical value of the stress intensity factor that we obtained form our analysis, and the comparison of numerical values must be made with caution. Furthermore the sample used by Broz et al (2006) had a perthitic microstructure and may differ in its mechanical properties from our gem-quality sanidines, which are chemically and structurally homogeneous down to the nm scale. Finally, due to the potential contribution of the lattice strain associated with chemical alteration next to the crack walls, there is also some uncertainty with our experiments, which has not yet been evaluated. Nevertheless, we think that our experiments do present an interesting alternative to conventional mechanical testing which rests on a well defined geometry of the crack pattern for which analytical solutions or approximations are available (Tada et al. 2000).
Since K_I is nearly independent of crack length at $s \geq 0.3$, which is characteristic for the observed crack patterns, the crack length cannot be predicted

using equation (3). The growth of an initial crack (say a crack with $s \geq 0.3$) is controlled by the stability behavior of the growth process itself as it has been treated in the literature. We refer to e.g. Muhlhaus (1996) and do not concentrate on this aspect.
Finally, the question arises up to the reason for the approximately 18^o orientation mismatch between the plane normal of the cracks and the direction of maximum tensile stress. There is no obvious relation to the anisotropy of the crystal's bonding system as represented in terms of periodic bond chains. However, the crack plane almost coincides with the plane defined by the directions of the two pronounced maxima of the longitudinal elastic stiffness (see Figure 11). One maximum points into the b-direction, the other lies in the a-c plane pointing into a direction that encloses an angle of approximately 78^o with the negative a axis measured towards the positive c axis. Thus, the longitudinal elastic stiffness is generally high in a plane that is subparallel to the cracks (Figure 11) and has its lowest values in the direction sub-perpendicular to the cracks. Although the atomistic mechanisms underlying this relation are not known, it appears likely that the anisotropy of the longitudinal elastic stiffness at least partially controls the orientation of the cracks and is responsible for the mismatch between the crack normal and the direction of maximum tensile stress.

Conclusions

It has been confirmed experimentally that fracturing in alkali feldspar may occur due to coherency stress associated with composition change in the course of Na^+-K^+ cation exchange. This phenomenon is due to a substantial composition dependence of the lattice parameters of alkali feldspar and its marked anisotropy. The mechanical analysis of a thin misfitting surface layer under tensile stress, that is the situation corresponding to a composition shift towards more sodium-rich compositions, delivers an estimate of ≈ 325 MPa for the critical tensile stress needed to initiate mode I cracks. The regularity of systems of parallel cracks that emanate from polished (010) and (001) surfaces indicates that the characteristic spacing between cracks is controlled by the induced coherency stress rather than by irregularly distributed defects or flaws in the crystal structure. This allows extraction of the stress intensity factor, $K_I = 2.3$ MPa m$^{1/2}$/73 MPa mm$^{1/2}$ to 2.72 MPa m$^{1/2}$/86 MPa mm$^{1/2}$ from the relation between characteristic crack spacing and induced stress. A slight orientation mismatch between the crack normal and the direction of maximum tensile stress is tentatively ascribed to the anisotropy of the longitudinal elastic stiffness. With our experiments on the chemically induced

fracturing in alkali feldspar an alternative means of investigating fracturing behavior in brittle materials is documented.

Acknowledgements

This work was funded by the Deutsche Forschungsgemeinschaft project AB 314/2-1 and by the Austrian Science foundation, FWF project I 474-N19, both in the framework of the research unit FOR 741-DACH. We are grateful to G. Giester and A. Wagner for their help in preparing oriented single crystal plates.

Appendix

Eigenstrain due to composition change

Let $\mathbf{r}$ and $\mathbf{R}$ indicate the position of a specific point in the crystal lattice before and after composition change, respectively,

$$\mathbf{r} = \left(x_1, x_2, x_3\right), \quad \mathbf{R} = \left(X_1, X_2, X_3\right)$$

The two vectors are related through the displacement vector $\mathbf{u}(\mathbf{r})$

$$\mathbf{R} = \mathbf{r} + \mathbf{u}(\mathbf{r}).$$

The associated strain tensor ε_{ij} is defined as a symmetric sum

$$\varepsilon_{ij} = \frac{1}{2}(I_{ij} + I_{ji}) \quad \text{with} \quad I_{ij} = \frac{\partial u_i}{\partial x_j},$$

where I_{ij} denotes the displacement gradient. If the strain is homogeneous, $I_{ij} = \text{const}$, one can explicitly find the components of $\mathbf{u}(\mathbf{r})$

$$u_i = I_{ij} x_j, \quad X_i - x_i = I_{ij} x_j.$$

The linear transformation from $\mathbf{r}$ to $\mathbf{R}$ can now be written in a compact matrix notation

$$\mathbf{R} = M\mathbf{r}, \quad M = I + id \tag{4}$$

where id denotes the 3×3 identity matrix.
We now consider a monoclinic coordinate system with axes $\mathbf{a}$, $\mathbf{b}$, $\mathbf{c}$ and corresponding angles $\alpha = \gamma = 90°$, $\beta \neq 90°$. Let $\mathbf{i}$, $\mathbf{j}$, $\mathbf{k}$ be the unit vectors along the Ox, Oy, and Oz axes of the orthogonal coordinate system, and

let the monoclinic coordinate system be oriented such that $\mathbf{a} \parallel Ox$, $\mathbf{b} \parallel Oy$, $\mathbf{c}^\star \parallel Oz$ (see figure 12). The vectors $\mathbf{a}$, $\mathbf{b}$, and $\mathbf{c}$ can be related to $\mathbf{i}$, $\mathbf{j}$, $\mathbf{k}$ by the matrix equation

$$\begin{pmatrix} \mathbf{a} \\ \mathbf{b} \\ \mathbf{c} \end{pmatrix} = \begin{pmatrix} a & 0 & 0 \\ 0 & b & 0 \\ c\cos\beta & 0 & c\sin\beta \end{pmatrix} \begin{pmatrix} \mathbf{i} \\ \mathbf{j} \\ \mathbf{k} \end{pmatrix} = S \begin{pmatrix} \mathbf{i} \\ \mathbf{j} \\ \mathbf{k} \end{pmatrix},$$

where $S = S(a, b, c, \beta)$ is the transformation matrix. In what follows we denote $S(a_0, b_0, c_0, \beta_0)$ by S_0 and $S(a_1, b_1, c_1, \beta_1)$ by S_1.
For the vector $\mathbf{r}$ we have

$$\mathbf{r} = \begin{pmatrix} x_1 & x_2 & x_3 \end{pmatrix} \begin{pmatrix} \mathbf{i} \\ \mathbf{j} \\ \mathbf{k} \end{pmatrix} = \begin{pmatrix} m & n & p \end{pmatrix} \begin{pmatrix} \mathbf{a}_0 \\ \mathbf{b}_0 \\ \mathbf{c}_0 \end{pmatrix} = \begin{pmatrix} m & n & p \end{pmatrix} S_0 \begin{pmatrix} \mathbf{i} \\ \mathbf{j} \\ \mathbf{k} \end{pmatrix},$$

such that

$$\begin{pmatrix} x_1 \\ x_2 \\ x_3 \end{pmatrix} = S_0^T \begin{pmatrix} m \\ n \\ p \end{pmatrix}.$$

Similarly, the components of $\mathbf{R}$ with respect to $Oxyz$ are related to the components referring to the monoclinic system through

$$\begin{pmatrix} X_1 \\ X_2 \\ X_3 \end{pmatrix} = S_1^T \begin{pmatrix} m \\ n \\ p \end{pmatrix} = S_1^T (S_0^{-1})^T \begin{pmatrix} x_1 \\ x_2 \\ x_3 \end{pmatrix} = (S_0^{-1} S_1)^T \begin{pmatrix} x_1 \\ x_2 \\ x_3 \end{pmatrix},$$

such that

$$\mathbf{R} = (S_0^{-1} S_1)^T \mathbf{r}. \tag{5}$$

Comparing Eqs. 4 and 5 we obtain an explicit expression for M

$$M = (S_0^{-1} S_1)^T.$$

For the displacement gradient we thus have

$$I = (S_0^{-1} S_1)^T - id,$$

and the strain tensor reads

$$\varepsilon = \frac{S_0^{-1} S_1 + (S_0^{-1} S_1)^T}{2} - id.$$

For the case at hand the components of the strain tensor are calculated as

$$\begin{pmatrix} \dfrac{a_1}{a_0} - 1 & 0 & \dfrac{c_1 \cos\beta_1}{2c_0 \sin\beta_0} - \dfrac{a_1 \cos\beta_0}{2a_0 \sin\beta_0} \\ 0 & \dfrac{b_1}{b_0} - 1 & 0 \\ \dfrac{c_1 \cos\beta_1}{2c_0 \sin\beta_0} - \dfrac{a_1 \cos\beta_0}{2a_0 \sin\beta_0} & 0 & \dfrac{c_1 \sin\beta_1}{c_0 \sin\beta_0} - 1 \end{pmatrix}.$$

References

Abart R, Petrishcheva E, Rhede D, Wirth R (2009a) Exsolution by spinodal decomposition II: Perthite formation during slow cooling of anatexites from Ngoronghoro, Tanzania. American Journal of Science 309: 450-475, 10.2475/06.2009.02

Abart R, Petrishcheva E, Kässner S, Milke R (2009b) Perthite microstructure in magmatic alkali feldspar with oscillatory zoning;Weinsberg Granite, Upper Austria. Mineralogy and Petrology 97: 251-263, 10.1007/s00710-009-0090-1

Angel R, Sochalski-Kolbus LM, Tribaudino M (2012) Tilts and tetrahedra: The origin of the anisotropy of feldspars. American Mineralogist, 97: 765-778.

Benisek A, Dachs E, Kroll H (2010) A ternary feldspar-mixing model based on calorimetric data: development and application. Contributions to Mineralogy and Petrology, 160, 327-337.

Bernardo E, Doyle J, Hampshire S (2007) Sintered feldspar glass ceramics and glass - ceramic matrix composites. Ceramics International, 34: 2037 - 2042.

Beuth, JL, (1992) Cracking of thin bonded films in residual tension. Int. Journ. Solids. Struct., 29, 1657-1675.

Brown W.L, Parsons I (1988) Zoned ternary feldspars in the Klokken intrusion: exsolution microtextures and mechanisms. Contributions to Mineralogy and Petrology 98: 444 - 454

Broz ME, Cook RF, Whitney DL. (2006) Microhardness, toughness, and modulus of Mohs scale minerals. American Mineralogist, 91: 135-142.

Demtroeder (2011) Untersuchung zur Al/Si-Ordnung an Sanidin-Megakristallen aus der Eifel. unpublished MSc Thesis Ruhr-Universität Bochum.

Fuhrman ML, Lindsley DH (1988) Ternary-feldspar modeling and thermometry. Am Mineral 73:3 - 4

Gross D, Seelig Th. (2001) Bruchmechanik mt Einführugn in die ???, 3'rd

Ed., Springer

Hovis GL, Delbove F, Bose MR. (1991) Gibbs energies and entropies of K-Na mixing for alkali feldspar from phase equilibrium data: implications for feldspar solvi and short range order. Am Mineral 76:913 - 927

Jamtveit B, Putnis C, Malthe-Sorenssen A (2009) Reaction induced fracturing during replacement processes. Contrib Mineral Petrol 157: 127-133, DOI 10.1007/s00410-008-0324-y.

Kroll H, Ribbe PH (1983) Lattice parameters, composition and Al,Si order in alkali feldspars. In PH Ribbe (ed): Feldspar Mineralogy. Reviews in Mineralogy 2: 57-100

Kroll H, Schmiemann I, von Coelln G (1986) Alklai feldspar solid-solutions. American Mineralogist 71: 1-16

Muhlaus HB, Chou KT, Ord A. (1996) Bifurkation crack pattern in arrays of two-dimensional cracks.Internatinal Journal of Fracture 77: 1-14

Neusser G, Abart R, Fischer FD, Harlov D, Norberg N. (2011) Experimental Na/K exchange between alkali feldspar and an NaCl - KCl salt melt: chemically induced fracturing and element partitioning. Contrib Mineral Petrol 164: 341 - 358

Norberg N, Neusser G, Wirth R, Harlov D (2011) Microstructural evolution during experimental albitization of K-rich alkali feldspar. Contrib Mineral Petrol 162: 531 - 546, DOI 10.1007/s00410-011-0610-y

Nye, J.P. (1985) Physical Properties of crystals, Oxford University Press, New York

Passchier CW, Trouw RJ (2005). Microtectonics. Springer, Heidelberg.

Petrishcheva E, Abart R. (2009) Exsolution by spinodal decomposition I: evolution equation for binary mineral solutions with anisotropic interfacial energy. American Journal of Science 2009; 309:431 - 49

Petrishcheva E, Abart R. (2012) Exsolution by spinodal decomposition for multicomponent mineral solutions, Acta Materialia, 60, 5481 - 5493.

Petrovic R (1973) Effect of coherency stress on mechanism of reaction albite+k+ reversible k-feldspar+na+ and on mechanical state of resulting feldspar. Contrib Mineral Petrol 41: 151-170

Putnis A (2002) Mineral replacement reactions: from macroscopic observations to microscopic mechanisms. Mineral Mag 66: 689-708

Putnis A (2009) Mineral Replacement Reactions. Rev Mineral and Geochem 70: 87-124

Quinn GD, Bradt R (2007) On the Vickers indentation fracture toughness test. Journal of the American Ceramic Society, 90: 673-680.

Robin P (1974) Stress and strain in cryptoperthite lamellae and the coherent solvus of alkali feldspar. Am Mineral, 59: 1299-1318

Schreuer J, Sondergeld P, Demtröder K (in prep.) Elastic properties of monoclinic alkali feldspars up to 1370 K. Phys. Chem. Min., in preparation

Schultz RA, Jensen MC, Bradt, RC. (1994) Single crystal cleavage of brittle materials, International Journal of Fracture, 65, 291-312.

Smith JV, Brown W (1988) Feldspar Minerals, Volume 1: Crystal Structures, Physical, Chemical, and Microtextural Properties: Berlin, Springer Verlag, 828 p.

Tada H, Paris PC, Irwin GR. (2000) The stress analysis of cracks handbook, 3rd ed., ASME Press/Professional Engineering Publishing/ASM

Thompson .JB. Jr, Waldbaum DR (1968) Mixing properties of sanidine crystalline solutions. I. Calculations based on ion-exchange data. Am Mineral 53: 1965-1999

Tullis J, Yund R (1979) Calculation of coherent solvi for alkali feldspar, iron-free clinopyroxene, nepheline-kalsilite, and hematite-ilmenite. Am Mineral 64: 1063-1074

Whitney DL, Broz ME, Cook RF (2006) Hardness, toughness, and modulus of some common metamorphic minerals. American Mineralogist, 92: 281-288.

Yund R (1984) Alkali Feldspar exsolution: Kinetics and dependence on alkali interdiffusion, in Brown, W. L., editor, Feldspars and feldspathoids: Structure, Properties, and Occurrences: Dordrecht, D. Reidel Publishing Company, NATO Advanced Science Institute Series C, v. 137:. 281-315

Figures

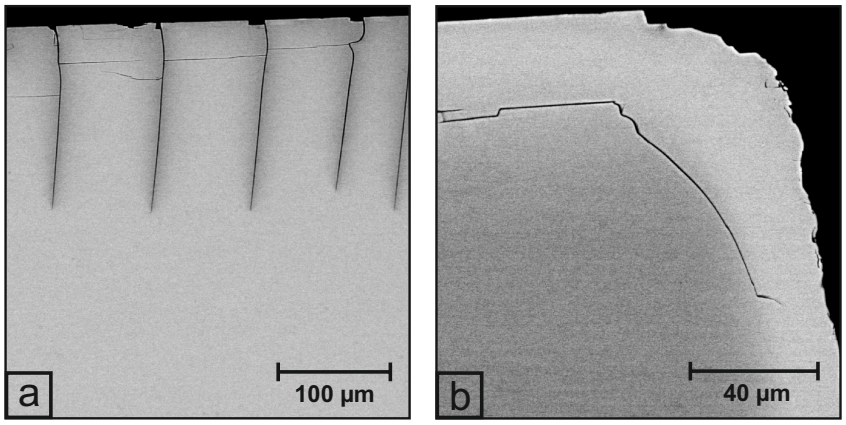

Figure 1: Cracks formed from Na^+-K^+ cation exchange between gem-quality sanidine from Volkesfeld and a NaCl-KCl salt-melt; run duration was 16 days: (a) BSE image of a system of parallel cracks emanating from a polished (001) surface of sanidine shifted from $X_{Or} = 0.84 \rightarrow 0.64$; the dark shades of grey along the cracks reflect low potassium contents in the exchanged portions; (b) BSE image of cracks along the transition zone between the alterated rim and the unexchanged core of a sanidine shifted from $X_{Or} = 0.84 \rightarrow 1.00$; the light grey shade in the outermost zone reflects the increased potassium content in the chemically altered domain.

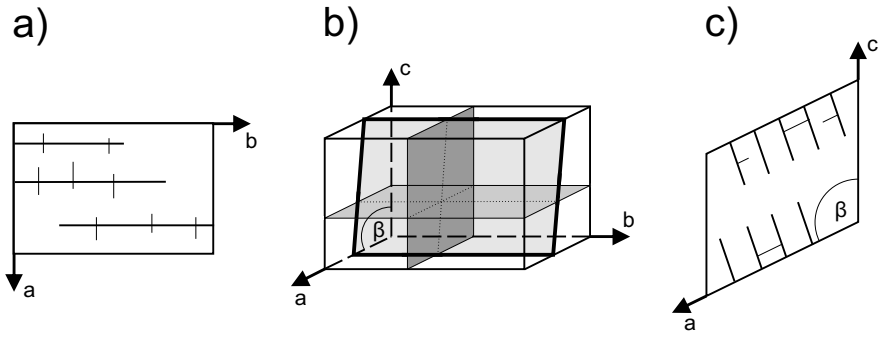

Figure 2: Schematic sketch of a plate with parallel cracks of the first hierarchical level and subordinate cracks of the second hierarchical level; (a) view onto the (001) surface, view direction parallel c^*; (b) oblique view, planes with light grey and dark grey shades represent cracks of the first- and second hierarchical level, respectively, (c) view onto the (010) surface, view direction parallel b.

Tables

Table 1: Representative chemical analyses of the starting materials; PR: Volkesfeld sanidine, EPR: Rockeskyller Kopf sanidine

phase	SiO_2	Al_2O_3	FeO	BaO	Na_2O	K_2O	MgO	Tot.	X_{Or}	X_{Ab}	X_{Cs}
PR	63.98	19.05	0.16	0.88	1.84	13.61	0.00	99.51	0.84	0.15	0.01
EPR	64.08	18.97	0.15	1.31	2.81	12.10	0.01	99.44	0.72	0.26	0.02

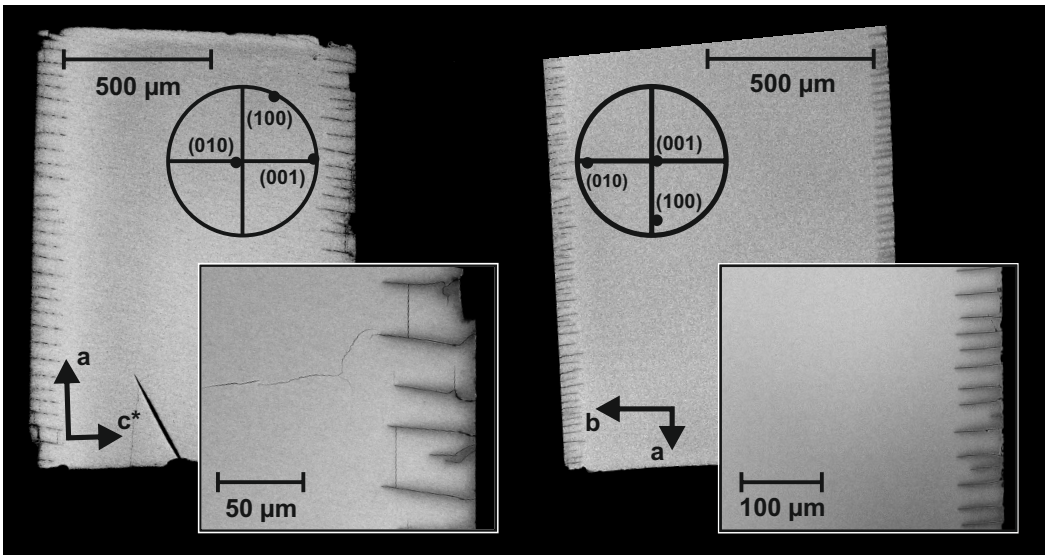

Figure 3: System of parallel cracks in a sanidine from Volkesfeld; run duration 8 days; (a) sanidine with polished (001) faces shifted from $X_{Or} = 0.84 \rightarrow 0.64$; view onto the (010) plane; (b) sanidine with polished (010) faces shifted from $X_{Or} = 0.84 \rightarrow 0.60$; view onto the (100) plane.

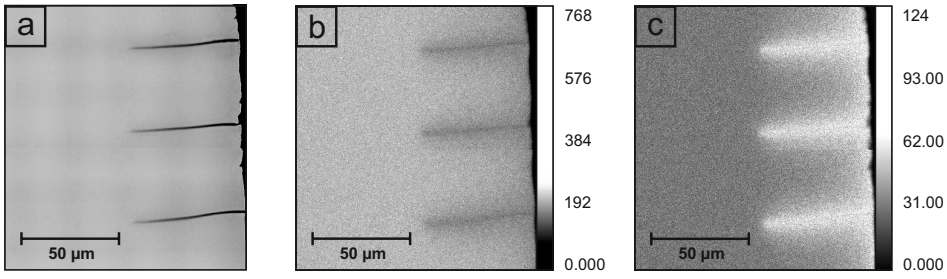

Figure 4: (a) BSE image; (b) K-distribution map, (c) Na-distribution map showing cracks with halos enriched in sodium and depleted in potassium indicating that the cracks indeed formed during cation exchange; numbers on the color lookup tables indicate counts per second.

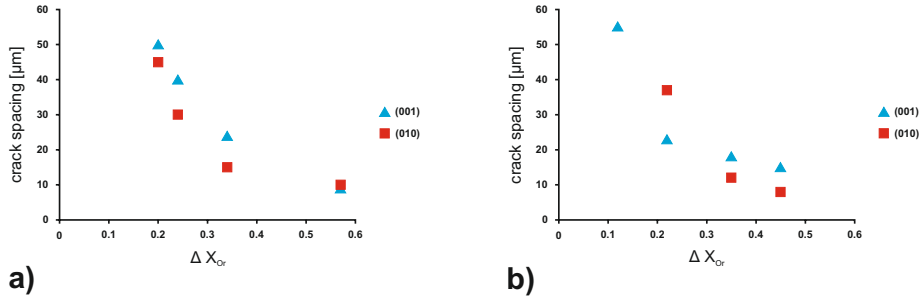

Figure 5: Crack spacing as a function of the chemical shift $\Delta X = X_{Or}^{init} - X_{Or}^{fin}$; (a) sanidine from Voklesfeld, $X_{Or}^{init} = 0.84$; (b) sanidine from the Rockeskyller Kopf, $X_{Or}^{init} = 0.72$.

Table 2: Results of the experiments conducted for determining the critical composition shift needed for initiation of fracturing.

label	X_{Or}^{init}	X_{KCl}	X_{Or}^{fin}	shift	cracks
SPR7-35-850	0.84	0.35	0.72	0.12	no
SPR7-34-850	0.84	0.34	0.71	0.13	yes
SPR7-33-850	0.84	0.33	0.69	0.15	yes
SPR7-32-850	0.84	0.32	0.68	0.16	yes
SPR7-31-850	0.84	0.31	0.66	0.18	yes

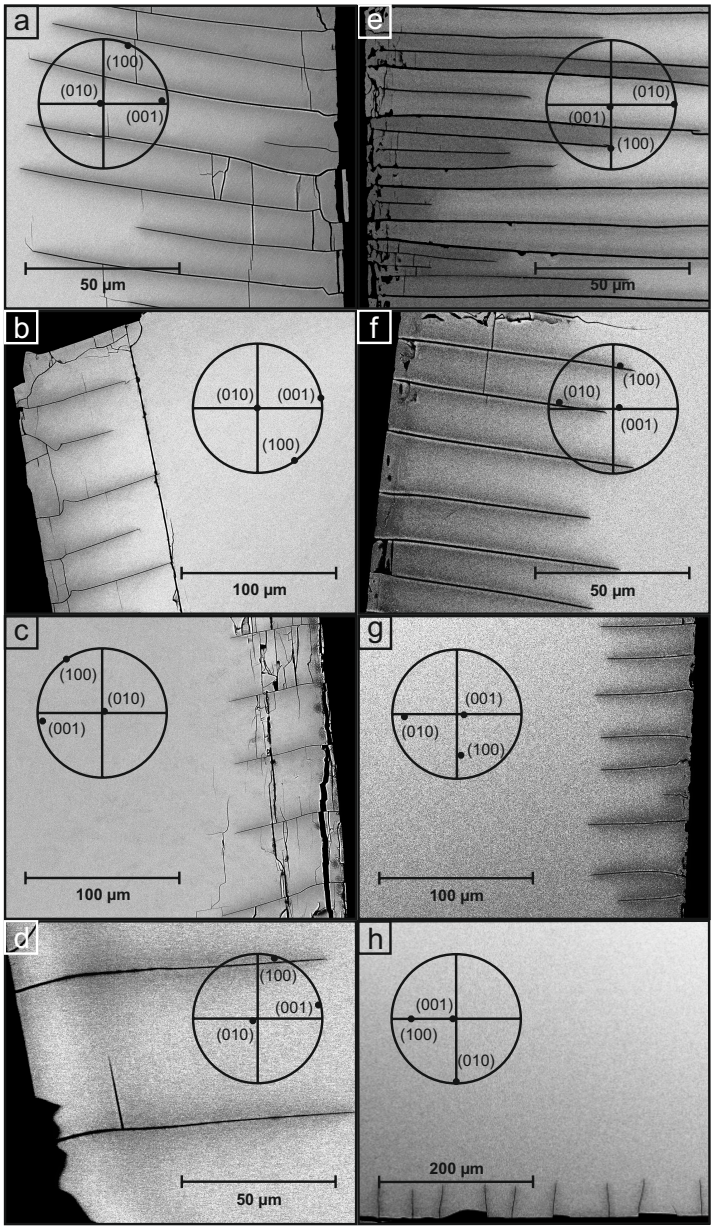

Figure 6: BSE images showing the relations between crack spacing and chemical shift in sanidine from Volkesfeld with initial X_{Or}=0,84; run duration: 7 days; the X_{KCl} of the salt melt was changed systematically; plate with (001) (a - d) and (010) (e - f) polished faces were used; (a) X_{Or} (exchanged) = 0.27; (b) X_{Or} (exchanged) = 0.50; (c) X_{Or} (exchanged) = 0.60; (d) X_{Or} (exchanged) = 0.64; (e) X_{Or} (exchanged) = 0.27; (f) X_{Or} (exchanged) = 0.50; (g) X_{Or} (exchanged) = 0.60 (h) X_{Or} (exchanged) = 0.64.

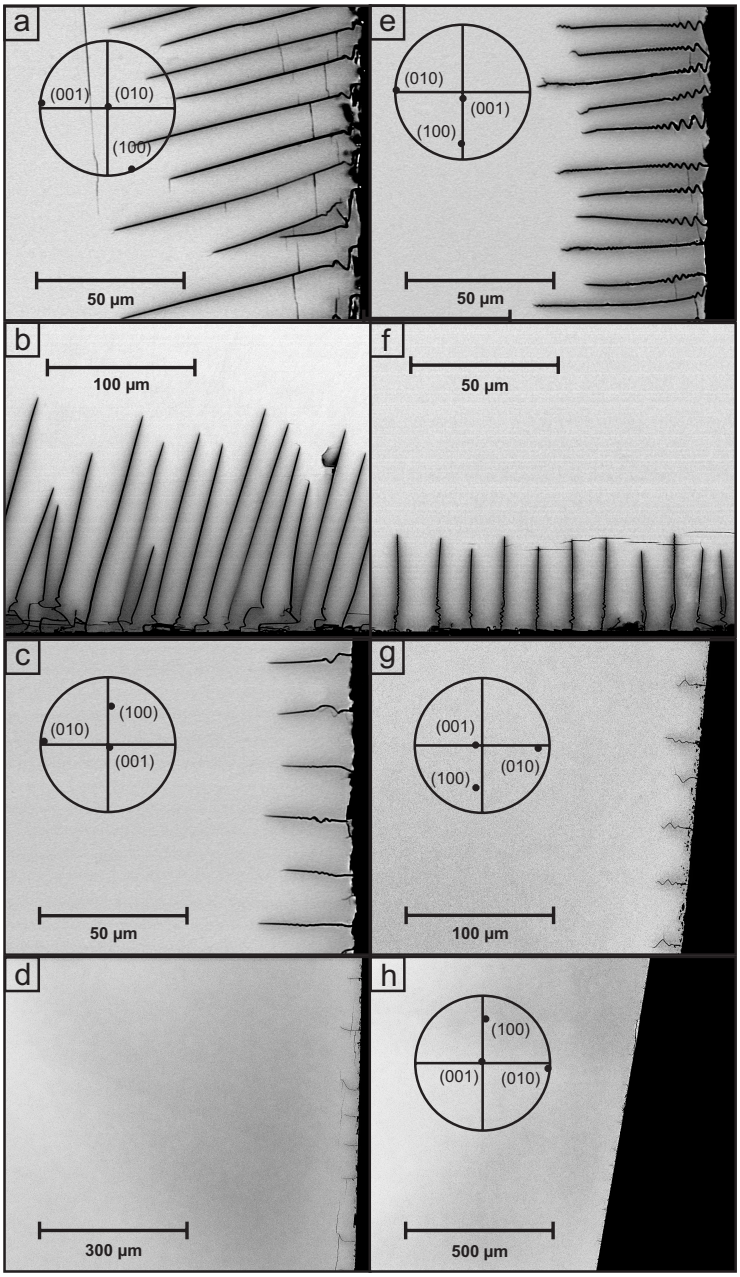

Figure 7: BSE images showing the relations between crack spacing and chemical shift in sanidine from Rockeskyller Kopf with initial X_{Or}=0,72; run duration: 7 days; the X_{KCl} of the salt melt was changed systematically; plates with (001) (a - d) and (010) (e - f) polished faces were used; (a) X_{Or} (exchanged) = 0.27; (b) X_{Or} (exchanged) = 0.50; (c) X_{Or} (exchanged) = 0.60; (d) X_{Or} (exchanged) = 0.64; (e) X_{Or} (exchanged) = 0.27; (f) X_{Or} (exchanged) = 0.50; (g) X_{Or} (exchanged) = 0.60 (h) X_{Or} (exchanged) = 0.64.

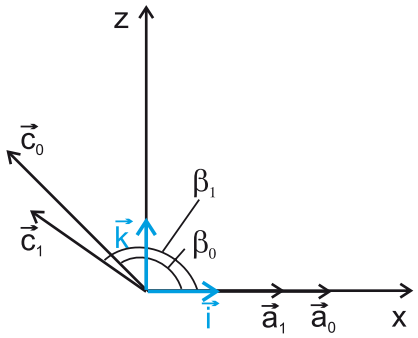

Figure 8: Monoclinic coordinate system with unit vectors $\mathbf{a}_0$, $\mathbf{b}_0$, $\mathbf{c}_0$ and angle β_0 before and $\mathbf{a}_1$, $\mathbf{b}_1$, $\mathbf{c}_1$ and angle β_1 after transformation; view direction is along the positive crystallographic b-axes; also shown is the orthogonal coordinate system $Oxyz$ with $Ox \parallel \mathbf{a}$, $Oy \parallel \mathbf{b}$, $Oz \parallel \mathbf{c}^\star$.

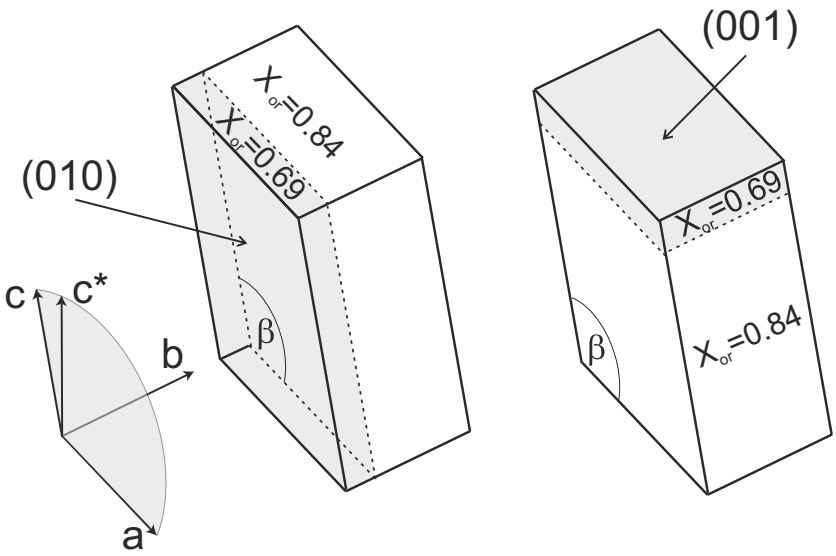

Figure 9: Schematic sketch of the geometric setting of a misfitting surface layer on a (010) (left) and (001) (right) surface of alkali feldspar.

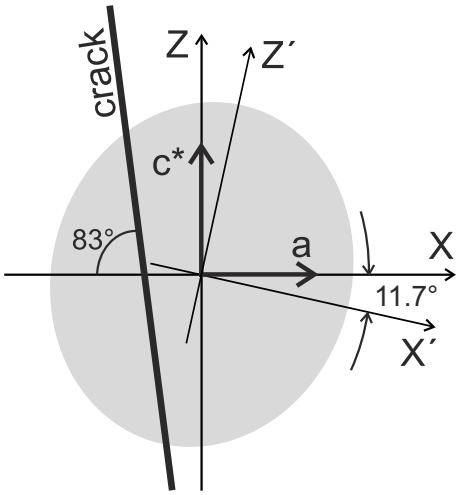

Figure 10: Crack direction and representation quadric of the stress tensor in the $x - z$ plane; X' and Z' correspond to the direction of σ_1 and σ_3, i.e., to the directions of maximum and minimum tensile stress, respectively, in the (010) plane.

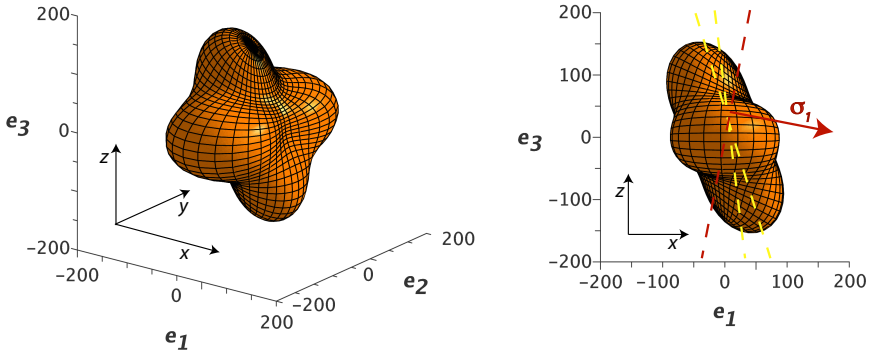

Figure 11: Representation surface of longitudinal elastic stiffness [GPa] (Schreuer et al in prep.), yellow dashed lines indicate range of observed crack orientations, red arrow indicates direction of maximum tensile stress σ_1, dashed red line: trace of normal plane to the direction of maximum tensile stress.

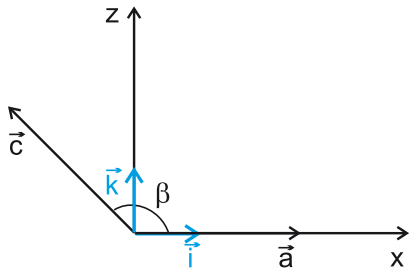

Figure 12: Monoclinic and orthogonal coordinate systems with **a** ∥ Ox, **b** ∥ Oy, **c*** ∥ Oz viewed down the crystallographic b-axes, **i**, **j**, **k** are the unit vectors along the Ox, Oy, and Oz axes.

Table 3: Relation between crack spacing and chemical shift; AS: apparent crack spacing; AA: apparent crack angle; CS: crack spacing; CL crack length.

label	polished faces	X_{Or} init.	X_{KCl} melt	X_{Or} exch.	shift	AS [μm]	AA [μm]	CS [μm]	CL [μm]
PR8-20-850	(001)	0.84	0.20	0.27	0.57	14	80	9	101
PR8-25-850	(001)	0.84	0.25	0.50	0.34	24	83	24	82
PR8-28-850	(001)	0.84	0.28	0.60	0.24	40	83	40	65
SP8-30-850	(001)	0.84	0.30	0.64	0.20	50	83	50	104
PRb8-20-850	(010)	0.84	0.20	0.27	0.57	10	7	10	151
PRb8-25-850	(010)	0.84	0.25	0.50	0.34	15	7	15	80
PRb8-28-850	(010)	0.84	0.28	0.60	0.24	30	7	30	62
SPb-30-850	(010)	0.84	0.30	0.64	0.20	45	7	45	46
EPR8-20-850	(001)	0.72	0.20	0.27	0.45	15	73	15	80
EP8-22-850	(001)	0.72	0.22	0.37	0.35	18	73	18	100
EPR8-25-850	(001)	0.72	0.25	0.50	0.22	23	73	23	32
EPR8-28-850	(001)	0.72	0.28	0.60	0.12	55	73	55	28
EPRb8-20-850	(010)	0.72	0.20	0.27	0.45	8	17	8	80
EPb8-22-850	(010)	0.72	0.22	0.37	0.35	23	17	12	32
EPRb8-25-850	(010)	0.72	0.25	0.50	0.22	35	17	37	21
EPRb8-28-850	(010)	0.72	0.28	0.60	0.12	145	17	152	18

Table 4: Instrument setting and standard materials used for reference in electron microprobe analysis

element	spectrometer crystal	standard	counting time peak [s]	counting time peak [s]
Na	TAP	Albite	8	4
K	PET	Orthoclase	8	4
Fe	LIF	Almandine	20	10
Ba	PET	BaSO4	25	15
Mg	TAP	Olivine	20	10
Al	TAP	Almandine	8	4
Si	TAP	Quartz	15	7.5

Table 5: Composition dependence of lattice parameters after Kroll et al. (1986)

	$X_{Or} = 0.85$	$X_{Or} = 0.69$
a [Å]	8.54	8.47
b [Å]	13.026	13.02
c [Å]	7.171	7.168
β	115.99°	116.01°

Table 6: Elastic constants [GPa] from J. Schreuer et al. (in prep.) referring to the standard orientation $Ox \parallel a$, $Oy \parallel b$ (diad axis), $Oz \parallel c^\star$ and calculated for $T = 850°$ C.

	$c_{i,1}$	$c_{i,2}$	$c_{i,3}$	$c_{i,4}$	$c_{i,5}$	$c_{i,6}$
$c_{1,j}$	61.8	43.8	34.0	0	-4.4	0
$c_{2,j}$	43.8	159.5	14.6	0	1.5	0
$c_{3,j}$	34.0	14.6	129.2	0	-28.9	0
$c_{4,j}$	0	0	0	14.5	0	0.3
$c_{5,j}$	-4.4	1.5	-28.9	0	29.4	0
$c_{6,j}$	0	0	0	0.3	0	36.4